Journal of Catalysis **198,** 232–242 (2001)
doi:10.1006/jcat.2000.3125, available online at http://www.idealibrary.com on IDEAL®

Structure and Properties of Oxidative Dehydrogenation Catalysts Based on MoO_3/Al_2O_3

Kaidong Chen, Shuibo Xie, Alexis T. Bell,[1] and Enrique Iglesia[1]

Chemical and Materials Sciences Divisions, E.O. Lawrence Berkeley National Laboratory, and Department of Chemical Engineering, University of California at Berkeley, Berkeley, California 94720-1462

Received July 12, 2000; revised November 8, 2000; accepted November 28, 2000; published online February 13, 2001

The effects of MoO_x structure on propane oxidative dehydrogenation (ODH) rates and selectivity were examined on Al_2O_3-supported molybdenum oxide catalysts with a wide range of Mo surface density (0.4–12 Mo/nm^2). X-ray diffraction and Raman, UV-visible, and X-ray absorption spectroscopies showed that the structure of dispersed molybdena depends strongly on the Mo surface density. Two-dimensional MoO_x oligomers formed preferentially for Mo surface densities below 4 Mo/nm^2. At higher surface densities, these MoO_x oligomers coexist on Al_2O_3 surfaces with three-dimensional MoO_3. UV-visible edge energies decrease with increasing Mo surface density, consistent with the growth of MoO_x structures. The evolution of near-edge spectral features in the X-ray absorption spectra and the gradual appearance of a Mo–Mo scattering peak in the radial structure function confirmed the growth of MoO_x domains with increasing surface density. ODH rates per Mo atom increased with increasing Mo surface density and reached a maximum value for samples with ~4.5 Mo/nm^2; this behavior reflects an increase in the reactivity of surface Mo species, because all MoO_x species are exposed at domain surfaces in this surface density range. As also shown for VO_x-based catalysts, turnover rates are higher on two-dimensional domains than on isolated monomers and they increase as the MoO_x domain size increases. The rates of reduction of MoO_x species in H_2 or C_3H_8 were probed using kinetic and X-ray absorption methods; these reduction rates increased in parallel with ODH rates as the MoO_x surface density increased, apparently as a result of the ability of larger domains to delocalize the higher electron density that accompanies the reduction process. As the surface density increased above 4.5 Mo/nm^2, ODH rates (per Mo atom) decrease, as a result of the loss of accessibility caused by the formation of MoO_3 crystallites. For these latter samples, the ODH rate per BET surface area approached a constant value as the surface density increased, because all exposed surfaces in these samples reside within two- or three-dimensional MoO_x structures with similar reactivity. The ratio of rate constants for propane ODH and propane combustion reactions increased with increasing surface density and then remained constant for values above 5 Mo/nm^2. These effects appear to reflect the tendency of Al–O–Mo species to adsorb alkoxide intermediates and favor their sequential oxidation to CO_x. Propene combustion rate constants also decreased relative to those for propane ODH as two-dimensional structures form with increasing Mo surface density.

INTRODUCTION

Many recent studies have explored the oxidative dehydrogenation of light alkanes as a potential new route to the corresponding alkenes. Oxidative dehydrogenation (ODH) of alkanes is favored thermodynamically and the presence of O_2 leads to the continuous removal of carbon deposits and to stable reaction rates. Secondary combustion reactions, however, limit alkene yields. Several studies have examined oxidative dehydrogenation pathways and the structure and active sites on the most active and selective catalysts (1–5), with the aim of minimizing combustion side reactions. Vanadia-based catalysts are among the most active and selective alkane ODH catalysts (3). Catalysts based on Mo oxides are widely used in selective alkene oxidation reactions, but they tend to be less active in alkane ODH reactions than VO_x-based catalysts (6–10). As a result, Mo catalysts tend to require higher temperatures than V catalysts, but several Mo–Mg–O catalysts show very high alkene selectivities (3, 7).

On both V-based and Mo-based catalysts, several studies of the kinetics and reaction mechanisms have shown that propane reactions occur via parallel and sequential oxidation steps (Scheme 1) (1–3, 11, 12). Propene forms via primary ODH reactions limited by the initial activation of the methylene C–H bond in propane (k_1), while CO and CO_2 (CO_x) can form via the combustion of the propene formed in step 1 (k_3) or the primary combustion of propane (k_2). The k_2/k_1 ratio (propane combustion/propane dehydrogenation) is generally low (~0.1) for selective ODH catalysts (13–15). The alkene yield losses observed with increasing conversion reflect large k_3/k_1 values (propene combustion/propane dehydrogenation ~10–50), which in turn arise from the weaker allylic C–H bond in propene relative to the methylene C–H bond in propane and from

[1] To whom correspondence should be addressed. E-mail: iglesia@cchem.berkeley.edu; bell@cchem.berkeley.edu.

0021-9517/01 $35.00

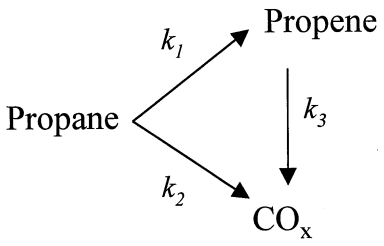

SCHEME 1. Reaction network in oxidative dehydrogenation of propane reactions.

the typically higher binding energy of alkenes on oxide surfaces (12–15).

Al_2O_3-supported MoO_3 catalysts have been widely used in hydrodesulfurization, hydrogenation, and alkene metathesis reactions. Few previous studies have addressed the reaction pathways and structural requirements for propane ODH reactions on MoO_x species supported on Al_2O_3 (8). The dispersion of MoO_x on Al_2O_3 has been studied in detail using complementary structural characterization techniques (16–26). These methods have shown that polymolybdate "monolayers" form on the Al_2O_3 surface with Mo surface densities of ~4.8 Mo/nm^2, either by sintering more dispersed MoO_x species into oligomeric domains or by the wetting of Al_2O_3 surfaces with mobile MoO_3 crystallites (25). As Mo surface densities exceed "monolayer" coverage, crystalline MoO_3 forms at low treatment temperatures (<873 K) and $Al_2(MoO_4)_3$ at higher temperatures (25).

This study addresses the effect of Mo surface density on the structure of MoO_x domains supported on Al_2O_3 and the relationship between their structure and their catalytic behavior in propane ODH. MoO_x/Al_2O_3 catalysts with different Mo surface densities (0.4–12 Mo/nm^2) were characterized by textural (BET), structural, and electronic probes (X-ray diffraction, Raman, UV-visible, and X-ray absorption spectroscopies). The reduction properties of MoO_x domains were determined by kinetic measurements of their initial reduction in H_2 and by *in situ* X-ray absorption studies after reduction in H_2 or C_3H_8. A detailed kinetic analysis of the reaction pathways in Scheme 1 was used to calculate rate constants for primary and secondary reactions from steady-state oxidative dehydrogenation rate data as a function of reactor residence time.

EXPERIMENTAL

Al_2O_3-supported MoO_x samples were prepared by incipient wetness impregnation of γ-Al_2O_3 (Degussa, AG) with a solution of ammonium heptamolybdate (AHM) (99%, Aldrich, Inc.) at a pH of 5. Impregnated samples were dried overnight in air at 393 K and then treated in dry air (Airgas, zero grade) at 773 K for 3 h.

Surface areas were measured by N_2 physisorption using a Quantasorb apparatus (Quantachrome Corporation) and standard multipoint BET analysis methods. Samples were evacuated at 383 K for 3 h before N_2 (Airgas, 99.999%) physisorption measurements. Powder X-ray diffraction patterns were obtained at room temperature using a Siemens diffractometer and Cu-$K\alpha$ radiation and a small powder sample mixed with Vaseline and spread on a thin glass plate.

Raman spectra were obtained using a HoloLab Series 5000 Raman spectrometer (Kaiser Optical) equipped with a Nd YAG laser frequency doubled to 532 nm. Samples (~50 mg) were pressed into wafers (0.9 cm diameter, 0.1 cm thickness) at 350 MPa and placed within a quartz cell (14). The laser was operated at a power level of 75 mW. The sample stage was rotated at 20 Hz in order to reduce the effect of laser heating on local temperatures (16). The Raman spectra of hydrated samples were recorded at ambient conditions. Samples were then treated at 673 K in 20% O_2/He for 1 h and cooled down to room temperature before the Raman spectra of these dehydrated samples were measured.

Diffuse reflectance UV-visible spectra were recorded using a Varian-Cary 4 spectrophotometer equipped with a Harrick diffuse-reflectance attachment. MgO was used as a reference. Reflectance measurements were converted to absorption spectra using the Kubelka–Munk function (27). UV-visible spectra were measured in the range of 1.5–5.0 eV at room temperature.

Mo K-edge X-ray absorption spectra (XAS) were measured using beamlines 4-1 and 2-3 at the Stanford Synchrotron Radiation Laboratory using an *in situ* flow cell (28). All samples were pressed into wafers, crushed, and sieved to retain particles with 0.18- to 0.25-mm diameter. These particles were placed into thin quartz capillaries (1.0-mm diameter; 0.1-mm wall thickness) and supported horizontally within the *in situ* cell (28) in the path of the rectangular X-ray beam (0.2 × 6.0 mm). Spectra were measured in transmission mode using a Si(220) crystals monochromator with 5-eV energy increments in the pre-edge region (19.875 to 19.975 keV), 0.25-eV increments in the edge region (19.975 to 20.035 keV), and 0.04 Å^{-1} in the fine structure region (20.035 to 21.024 keV). X-ray absorption data were analyzed using WinXAS software (version 1.2) (29). The energy was calibrated using the first inflection point in the Mo foil spectrum (19.999 keV).

MoO_x reduction rates were measured using a Quantasorb surface area analyzer (Quantachrome Corporation) modified with electronic mass flow meters as samples were heated in a 20% H_2/Ar mixture (1.33 cm^3 s^{-1}; Matheson UHP, certified mixture). The H_2 concentration in the effluent was measured by thermal conductivity detection after removing water with a 13X molecular sieve trap. Samples were held within a 4-mm-ID quartz cell containing a quartz thermowell directly in contact with the sample. Catalyst

amounts varied depending on their MoO_3 content in order to maintain the same amount of MoO_3 in each sample (5 mg). The H_2 concentration in the effluent was measured as the temperature was increased to 1200 K at 0.167 K s^{-1}. The thermal conductivity response was calibrated using the complete reduction of CuO powder (Aldrich, 99.995%).

Propane ODH rate and selectivity measurements were carried out at 703 K in a packed-bed tubular quartz reactor using 0.03- to 0.3-g samples. Propane (14 kPa; Airgas, 99.9%) and oxygen (1.7 kPa; Airgas, 99.999%) with He (Airgas, 99.999%) as a diluent were used as reactants. Reactants and products were analyzed by gas chromatography (Hewlett–Packard 5880 GC) using procedures described previously (13, 14). C_3H_8 and O_2 conversions were varied by changing reactant space velocity (F/w; w, catalyst mass; F, volumetric flow rate). Typical conversions were <2% for C_3H_8 and <20% for O_2. Initial ODH reaction rates and selectivities were obtained by extrapolation of these rate data to zero residence time. The effect of bed residence time on product yields was used in order to calculate rates and rate constants for secondary propene combustion reactions, using procedures reported previously (13, 14).

RESULTS AND DISCUSSION

Surface areas and Mo surface densities were measured for all MoO_x/Al_2O_3 samples after treatment in air at 773 K and the results are shown in Table 1. Mo surface density is expressed as the number of Mo atoms per square nanometer BET surface area (Mo atoms/nm^2). Surface areas decreased only slightly with increasing MoO_3 loading; therefore, the Mo surface density increased almost linearly with increasing MoO_3 concentration (Table 1).

Crystalline phases in MoO_x/Al_2O_3 samples were characterized by X-ray diffraction. No diffraction lines corresponding to Mo compounds were detected in samples with low Mo surface density (<5 Mo/nm^2), suggesting that MoO_x species are highly dispersed. MoO_3 diffraction lines appear

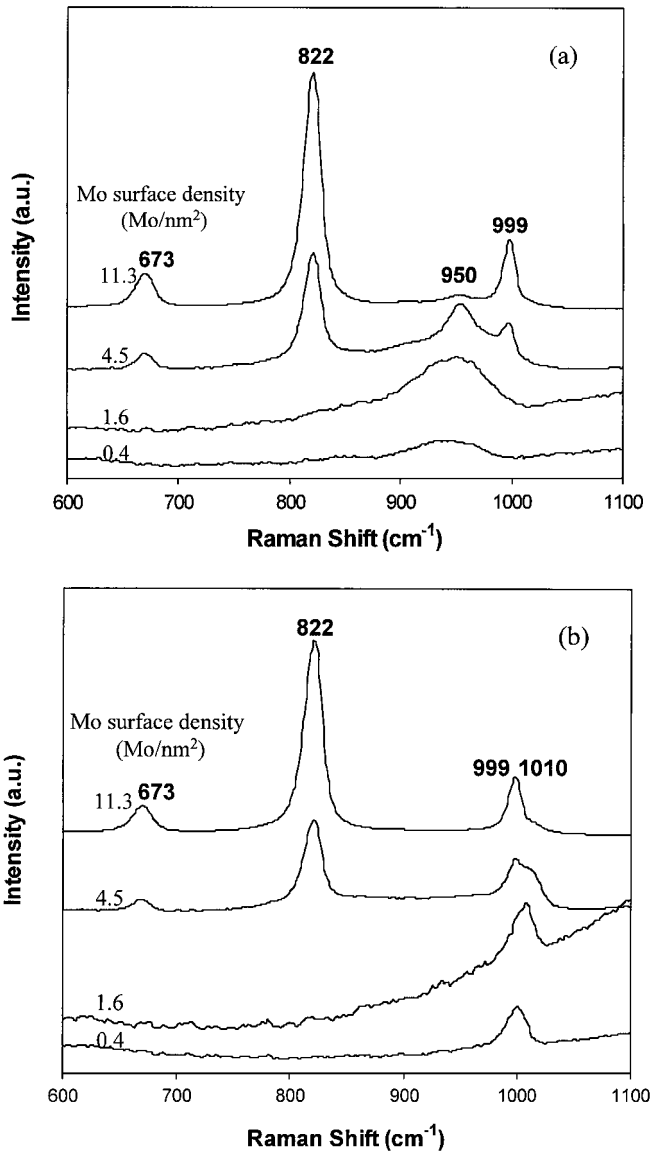

FIG. 1. Raman spectra of MoO_x/Al_2O_3 catalysts (a) under ambient conditions and (b) after treatment in 20% O_2/He at 673 K for 1 h.

TABLE 1

Surface Area and Mo Surface Density for MoO_x/Al_2O_3 Catalysts

MoO_3 loading (%)	Surface area (m^2/g)	Mo surface density (Mo/nm^2)
0	110	0
1	111	0.4
2	99	0.8
3	101	1.2
4	107	1.6
6	100	2.5
8	99	3.4
10	94	4.5
15	90	7.0
20	74	11.3

in samples with Mo surface densities greater than 7 Mo/nm^2. These results are consistent with geometric arguments that suggest the formation of a polymolybdate monolayer on Al_2O_3 at surface densities of ~4.8 Mo/nm^2 (24–26). No evidence for $Al_2(MoO_4)_3$ was detected in any of the samples, suggesting that the reaction between MoO_x and Al_2O_3 does not occur during treatment in air at 773 K.

Raman spectroscopy can detect changes in local structure within dispersed oxide domains by probing metal–oxygen vibrational modes. The Raman spectra for hydrated and dehydrated MoO_x/Al_2O_3 samples with different Mo surface densities are shown in Fig. 1. For samples with low Mo surface density (0.4 and 1.6 Mo/nm^2), only one broad band at ~955 cm^{-1} was observed (Fig. 1a); this band shifted to

$\sim$1010 cm^{-1} after dehydration (Fig. 1b). These bands are assigned to two-dimensional MoO_x oligomers dispersed on the Al_2O_3 surface (20, 21). The dispersed nature of MoO_x species at these low surface densities is consistent with the absence of crystalline structures in their X-ray diffraction patterns. At higher Mo surface densities ($\sim$4.5 Mo/nm^2), four bands appeared at 673, 822, 955, and 999 cm^{-1} in samples exposed to ambient air (hydrated). Dehydration by treatment in 20% O_2/He at 673 K for 1 h caused the band at $\sim$955 cm^{-1} to shift to 1010 cm^{-1}, while the frequencies of the other three bands remained unchanged. As noted above, these bands are assigned to two-dimensional MoO_x species. The Raman bands at 673, 822, and 999 cm^{-1} are typical of MoO_3 crystallites (16), and they are not influenced by hydration–dehydration processes. Thus, it appears that two-dimensional MoO_x oligomers and three-dimensional MoO_3 clusters co-exist on Al_2O_3 at surface densities of $\sim$4.5 Mo/nm^2. The absence of MoO_3 diffraction lines in these samples reflects the small size of the MoO_3 crystallites, which are detected by Raman because of the sensitivity of Mo–O vibrations to the local structure. For surface densities above 10 Mo/nm^2, the Raman bands for MoO_x oligomers at $\sim$955 cm^{-1} (hydrated sample) and $\sim$1010 cm^{-1} (dehydrated sample) become very weak, while the bands at 673, 822, and 999 cm^{-1} for MoO_3 crystallites become more intense. This increase in the relative abundance of three-dimensional MoO_3 structures is consistent with the detection of X-ray diffraction lines for crystalline MoO_3 at surface densities above 10 Mo/nm^2. Taken together, the Raman and X-ray diffraction evidence indicates that the surface of Al_2O_3 is predominantly covered by two-dimensional MoO_x species at Mo surface densities lower than $\sim$4.5 Mo/nm^2. At higher surface densities, MoO_3 crystallites coexist with two-dimensional MoO_x structures and the size of the crystallites increases with increasing surface density.

The UV-visible spectra of solids reflect the electronic structure of their valence and conduction bands, but the typically broad nature of the bands that arise from charge transfer electronic transitions in metal oxides makes their assignment to specific structural units difficult. The energy of the absorption edge is easier to determine and it provides a more convenient description of the electronic properties of metal oxides (30). The absorption edge in the UV-visible spectra for all MoO_x/Al_2O_3 samples was calculated using Tauc's law for indirect and amorphous semiconductors and previously reported procedures (31, 32). In this method, the absorption edge is defined as the x-intercept of the straight line describing the near-edge region for spectra plotted as $[F(R_\infty)h\nu]^{1/2}$ as a function of $h\nu$, where $F(R_\infty)$ is the Kubelka–Munk function (27) and $h\nu$ is the energy of the incident photon. The position of the absorption edge for low-energy charge-transfer transitions depends on the domain size of small semiconductor and insulator structures (32–39). The absorption edge energy decreases with increasing domain size. This relationship has recently been used to characterize the size of MoO_x (30), WO_x (32), and VO_x (13, 14) domains in dispersed structures useful as catalytic solids.

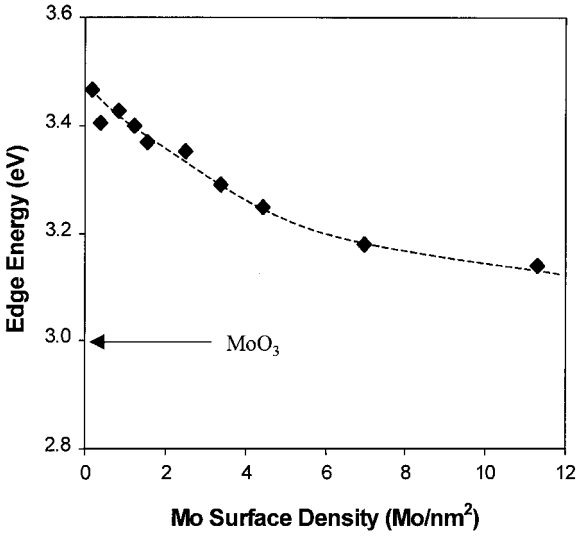

FIG. 2. Dependence of the UV-visible absorption edge energy on the Mo surface density of MoO_x/Al_2O_3 catalysts under ambient conditions.

The diffuse reflectance UV-visible spectra of MoO_x/Al_2O_3 samples were measured as a function of Mo surface density and the absorption edge energies were calculated as described above (Fig. 2). For Mo surface densities up to 12 Mo/nm^2, the absorption edge energy decreased monotonically with increasing Mo surface density (Fig. 2) and approached the value of $\sim$3 eV typical of large MoO_3 crystallites. This suggests that the size of MoO_x domains increases monotonically with increasing surface density (30), a trend that is consistent with the more qualitative evidence provided by Raman spectroscopy and X-ray diffraction data.

The structure of MoO_x/Al_2O_3 catalysts was also examined by X-ray absorption (XAS), which probes the local structure around absorber atoms within complex solids (40). Near-edge spectra (XANES) contains information about the oxidation state and coordination symmetry of the absorber, while the X-ray absorption fine structure provides details about the coordination of the absorber with neighboring atoms (40). In MoO_x samples, the Mo–K edge detected at 20.00 keV corresponds to the ejection of a Mo 1s electron, while the pre-edge feature at 19.99 keV arises from a 1s to 4d electronic transition that is dipole-forbidden in centrosymmetric structures. The Mo^{+6} centers in MoO_3 occupy off-center positions in MoO_6 octahedra and this distortion from perfect octahedral structures increases the extent of p–d orbital mixing, which renders these transitions allowed. The intensity of this pre-edge feature increases as the Mo^{+6} centers acquire tetrahedral symmetry, because of greater p–d orbital mixing (41).

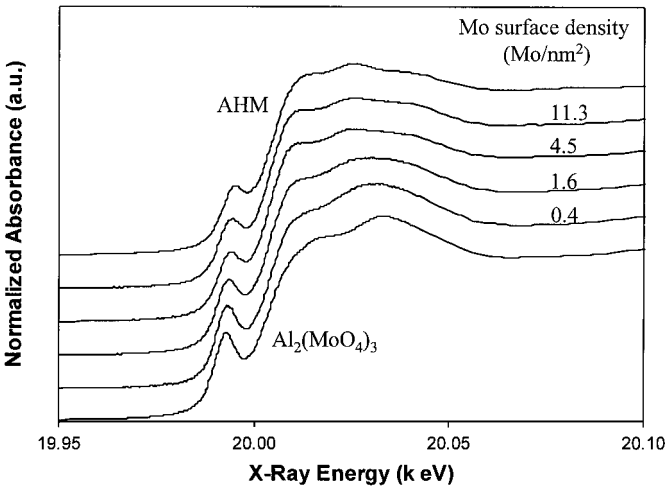

FIG. 3. Near-edge X-ray absorption spectra of alumina molybdate ($Al_2(MoO_4)_3$), ammonium heptamolybdate (AHM), and MoO_x/Al_2O_3 samples just after impregnation and drying in air at 393 K for 12 h.

Figure 3 shows the near-edge spectra of MoO_x/Al_2O_3 samples with different Mo surface densities after impregnation and drying in air at 393 K for 12 h. The spectra for two model compounds, aluminum molybdate ($Al_2(MoO_4)_3$) and ammonium heptamolybdate (AHM) are also shown in Fig. 3; these are representative structures for tetrahedral and octahedral coordination, respectively. The near-edge spectra for MoO_x/Al_2O_3 samples can be used to detect changes in the local structure and electronic properties of MoO_x by comparing them with near-edge spectra for appropriate reference compounds (22, 42–44). For MoO_x/Al_2O_3 samples with low Mo surface density, the pre-edge feature is relatively intense and the near-edge spectra resemble the spectrum for $Al_2(MoO_4)_3$ more than that for AHM, suggesting that at low Mo surface coverage, Mo atoms are mostly tetrahedral, consistent with the proposed dispersed nature of MoO_x domains in these samples. As the Mo surface density increases, the intensity of the pre-edge feature decreases and the spectral features gradually approach those typical of AHM, consistent with larger MoO_x domains and with a more octahedral structure. These results suggest that the MoO_x species formed during impregnation and drying become larger and more octahedral as the Mo surface density increases.

The XANES spectra of MoO_x/Al_2O_3 samples with Mo surface densities of 0.4–12 Mo/nm^2 were also measured after heat treatment in air at 773 K for 3 h. As also reported by Imamura *et al.* (22), these spectra did not show a clear change with Mo concentration; therefore, it is not possible to assess the MoO_x domain size in these samples. The reasons for the lack of sensitivity of these XANES spectra to the MoO_x domain size are not clear at this time.

The radial structure functions for MoO_x/Al_2O_3 samples after treatment in air at 773 K for 3 h are shown in Fig. 4. In all spectra, the largest feature at ~1.1 Å corresponds to scattering by the first Mo–O shell. A scattering peak at ~3.2 Å, corresponding to Mo–Mo next nearest neighbors, is clearly observed for the crystalline MoO_3 standard (22). For MoO_x/Al_2O_3 samples with low Mo surface density, this peak at ~3.2 Å was not observed, suggesting that MoO_x species exist within highly dispersed structures. As the Mo surface density increases, a Mo–Mo scattering peak emerged at 11.3 Mo/nm^2 surface density, indicating that MoO_x domains become progressively larger and acquire a larger number of next nearest neighbors with increasing Mo surface density. Together with the XANES results, these radial structure functions confirm the highly dispersed nature of MoO_x species at low Mo surface density proposed from XRD, Raman, and UV-visible data. These data also confirm the conclusions reached by these latter methods about the growth of MoO_x domains as surface density increases and about the incipient formation of MoO_3 as the polymolybdate monolayer capacity of Al_2O_3 is exceeded (at surface densities of ~4.5 Mo/nm^2).

Propane reaction rates and selectivities on MoO_x/Al_2O_3 are reported in Figs. 5–8. Figure 5 shows propane conversion and selectivity to propene as a function of residence time on a MoO_x/Al_2O_3 sample with a Mo surface density of 4.5 Mo/nm^2. Propene selectivities decreased as the propane conversion increased with increasing residence time, because of secondary combustion of propene to CO_x. The reaction rate constants (k_1, k_2, and k_3) in Scheme 1 can be calculated from these residence time effects (14). At the modest H_2O concentrations prevalent at the low conversions of these experiments, the rate of each reaction in Scheme 1 can be described accurately by

$$r_1 = k_1[C_3H_8] \quad [1]$$

$$r_2 = k_2[C_3H_8] \quad [2]$$

$$r_3 = k_3[C_3H_6], \quad [3]$$

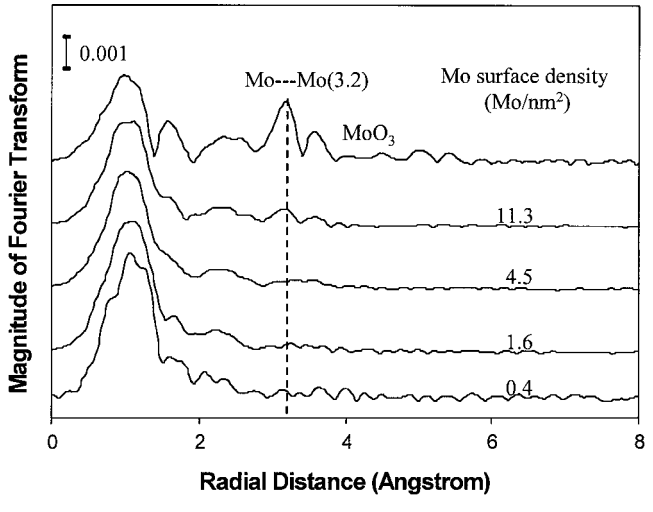

FIG. 4. Radial structure functions of bulk MoO_3 and of MoO_x/Al_2O_3 catalysts after treatment in air at 773 K for 3 h.

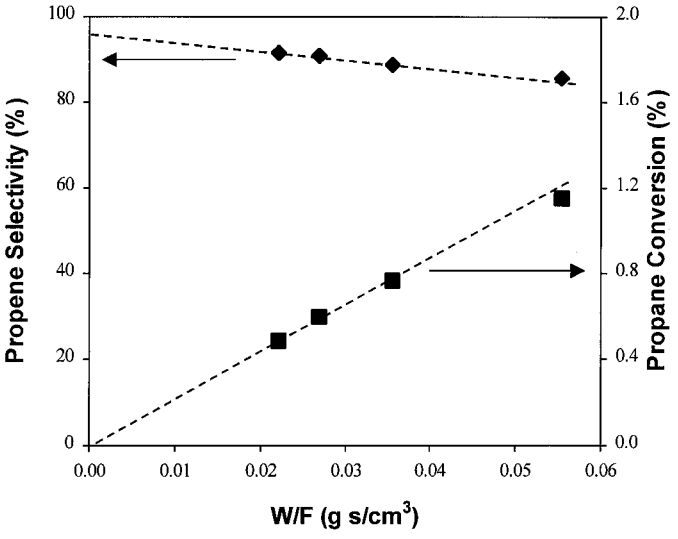

FIG. 5. Effects of bed residence time on propane conversion and propene selectivity (10 wt% MoO_x/Al_2O_3, 4.5 Mo/nm^2, 703 K, 14 kPa C_3H_8, 1.7 kPa O_2, balance He).

where k_i is the apparent first-order rate constant for each reaction i. The propene selectivity at relatively low O_2 and C_3H_8 conversions for the plug-flow hydrodynamics of the reactor used are accurately given by (14)

$$S = S^0[1 - (k_3 C_v/2)\tau], \qquad [4]$$

where C_v is the concentration of Mo atoms per unit reactor volume, τ is the reactor residence time, and $S^0 = k_1/(k_1 + k_2)$ is the initial propene selectivity (as $\tau \to 0$). The value of k_1 can be obtained from the initial rate of propene formation (as $\tau \to 0$) and the value of k_2 from the initial propene selectivity (S^0). The value of k_3 can be estimated from the effect of residence time on propene selectivity given by Eq. [4].

The data in Fig. 5 show that the selectivity to propene decreases with increasing propane conversion as a result of secondary combustion reactions that lead to the formation of CO_x. The propene selectivity at zero reactant conversion reflects the relative rates of propane ODH and combustion (reactions 1 and 2 in Scheme 1). Figure 6 shows that the initial propene selectivity increased with increasing Mo surface density until it reached a constant value of ~95% at surface densities higher than 5 Mo/nm^2. This gradual increase in C_3H_6 selectivity with MoO_x surface density suggests that Mo–O–Al sites or uncovered Al_2O_3 surfaces near MoO_x species may catalyze the unselective conversion of propane to CO_x. This may reflect, in turn, the tendency of such sites to bind alkoxide intermediates more strongly than Mo–O–Mo structures in polymolybdate domains or MoO_3 clusters. The complete coverage of the Al_2O_3 by a polymolybdate monolayer leads to a high initial propene selectivity, which resembles that in samples with predominately MoO_3 species. A similar increase in initial propene selectivity with increasing surface density of the active oxide was reported previously on VO_x/Al_2O_3 catalysts (13).

Figures 7a and 7b show the effects of Mo surface density on the values of k_2/k_1 and k_3/k_1. Propene yields during propane ODH reactions depend on both k_2/k_1 and k_3/k_1 ratios; smaller values of either one of these ratios lead to higher propene selectivity for a given propane conversion. The value of k_2/k_1 reflects the relative rates of propane combustion and dehydrogenation; therefore, the trends observed are similar to those discussed above for propene selectivities at zero reactant conversion. The values of k_2/k_1 decreased with increasing Mo surface density; they reached a minimum value of about 0.05 for surface densities greater than 5 Mo/nm^2.

The values of k_3/k_1 were much greater than unity (Fig. 7b) on all MoO_x/Al_2O_3 samples, indicating that propene combustion occurs much more rapidly than propane dehydrogenation. It is this large k_3/k_1 value that causes the strong observed effect of propane conversion on propene selectivity (Fig. 5). The values of k_3/k_1 (10–40) measured on these MoO_x/Al_2O_3 catalysts are similar to those measured on VO_x/Al_2O_3 catalysts at 603 K (13). The k_3/k_1 ratios decreased slightly with increasing Mo surface density and then remained constant for Mo surface densities greater than 5 Mo/nm^2. These large k_3/k_1 ratios reflect the weaker C–H bonds in propene compared to those in propane, as well as the higher binding energy of propene relative to propane on Lewis acid sites provided by Mo^{+6} cations present on MoO_3 surfaces (12).

Initial propane ODH reaction rates are reported in Figs. 8a and 8b as a function of Mo surface density for all MoO_x/Al_2O_3 samples. Propene formation rates normalized

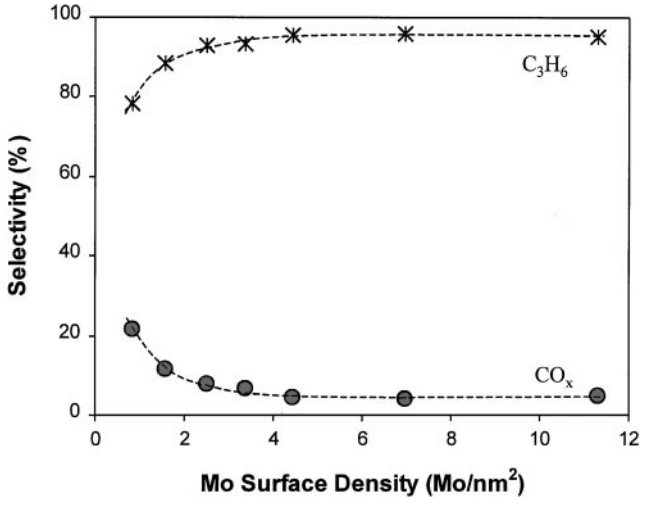

FIG. 6. Dependence of propene and CO_x selectivities on Mo surface density for MoO_x/Al_2O_3 catalysts (703 K, 14 kPa C_3H_8, 1.7 kPa O_2, balance He).

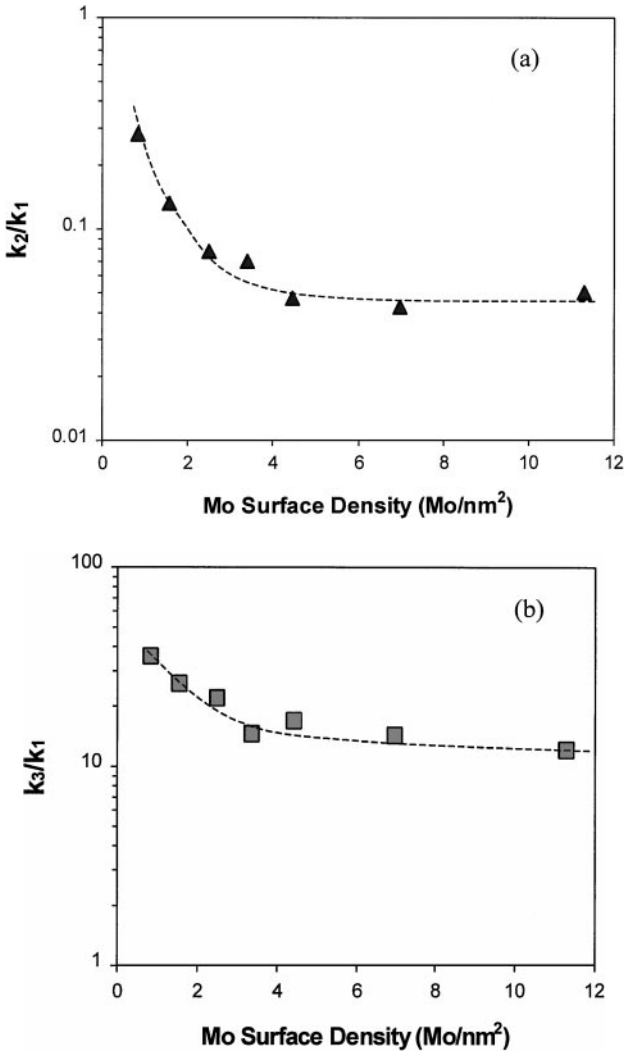

FIG. 7. Dependence of (a) k_2/k_1 and (b) k_3/k_1 values on Mo surface density for MoO_x/Al_2O_3 catalysts (703 K, 14 kPa C_3H_8, 1.7 kPa O_2, balance He).

per Mo atom initially increased with increasing Mo surface density and they approached maximum values at surface densities of ~4.5 Mo/nm^2 (Fig. 8a). In this range of surface density, the accessibility of MoO_x at domain surfaces is largely unaffected by Mo surface density, because the Al_2O_3 surface is covered predominantly by two-dimensional MoO_x oligomers. Therefore, the observed increase in reaction rate appears to reflect an increase in the reactivity (turnover rate) of exposed MoO_x active sites with increasing domain size. Propane dehydrogenation rates decrease as Mo surface densities exceed ~4.5 Mo/nm^2, which corresponds to the approximate surface density in a polymolybdate monolayer. The incipient appearance of three-dimensional MoO_3 structures, with the consequent incorporation of MoO_x into inaccessible positions within such clusters, is likely to account for the observed decrease in apparent turnover rates (Fig. 8a). Figure 8b shows initial propene formation rates normalized per BET surface area. These rates first increase with increasing Mo surface density, but above 5 Mo/nm^2, areal propene formation rates remain almost constant at higher Mo surface densities. Based on these results, we conclude that the initial increase in turnover rates for samples with two-dimensional structures of increasing domain size reflects the increasing reactivity and higher reducibility of MoO_x structures as oxide domains grow, as discussed in detail below. Similar domain size effects were observed on Al_2O_3-supported VO_x catalysts for propane ODH reactions (13). When Mo surface densities exceed monolayer coverage, three-dimensional MoO_3 form and the catalyst surface becomes fully covered by either two-dimensional MoO_x domains or MoO_3 clusters. Any additional Mo cations introduced become inaccessible for propane ODH; therefore, propane ODH

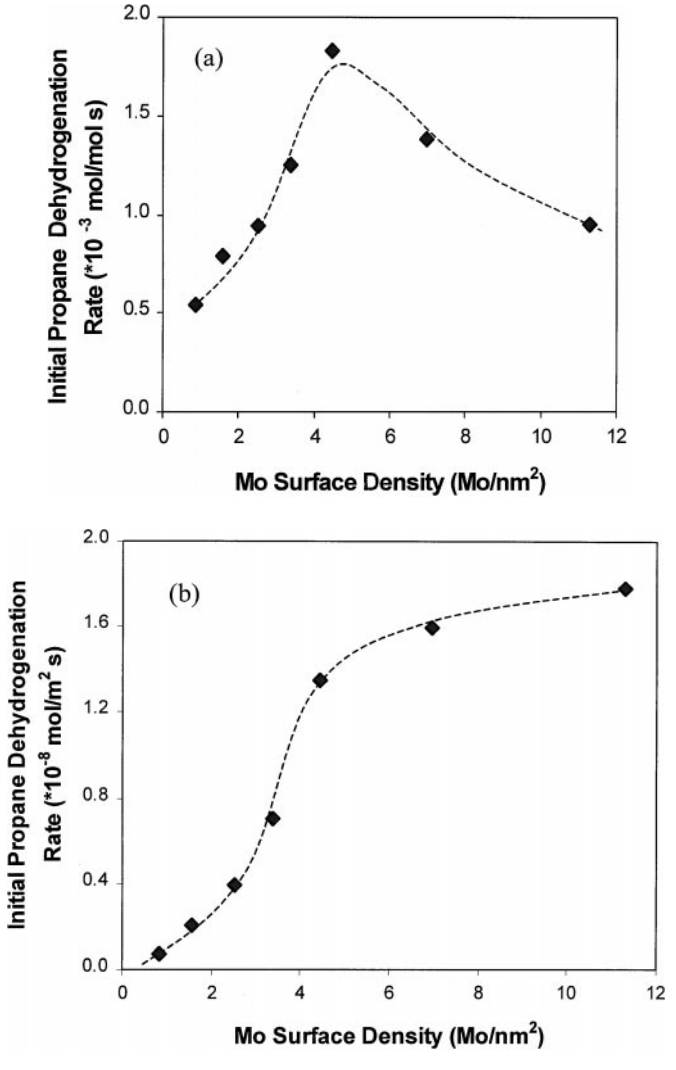

FIG. 8. Effects of Mo surface density on initial propene formation rates for MoO_x/Al_2O_3 catalysts (703 K, 14 kPa C_3H_8, 1.7 kPa O_2, balance He) (a) normalized per Mo atoms and (b) normalized per catalyst surface area.

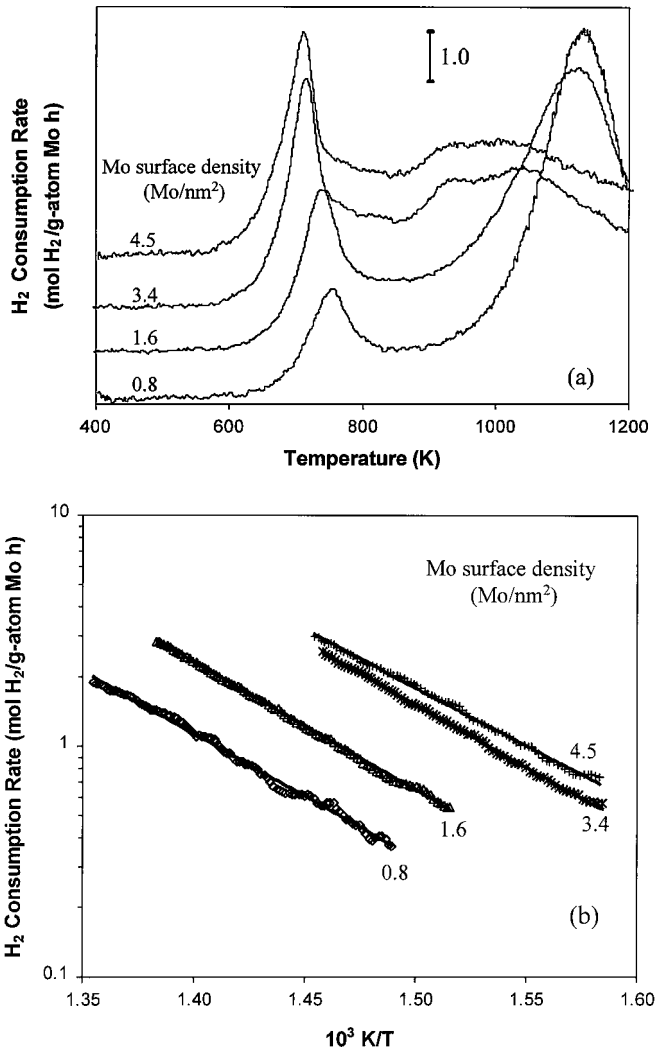

FIG. 9. (a) Temperature-programmed reduction profiles and (b) H_2 reduction rate as a function of temperature for MoO_x/Al_2O_3 catalysts (5 mg MoO_3, 20% H_2/Ar, 0.167 K s^{-1}).

rates normalized per Mo atom decrease, but the areal rate remains essentially constant.

Our recent kinetics and isotopic studies have confirmed previous suggestions that C–H bond activation steps using lattice oxygen limit the rate of propane ODH reactions on both MoO_x and VO_x catalysts (11, 12). C–H bond dissociation steps involve the incipient reduction of metal cations with the formation of a low surface density of oxygen vacancies during steady-state catalysis. As a result, the required activation barrier depends on the ability of metal oxide structures to form oxygen vacancies via the local reduction of metal centers (12). Such reduction processes require that the remaining oxide structure be able to accommodate two electrons, which remain after the removal of an oxygen atom. The ability of larger domains to delocalize charge more effectively may account for the higher reactivity of these larger domains in oxidation reactions.

On MoO_x and VO_x catalysts, propane ODH rates increase as the reducibility of the metal cations increase (12, 45–47). Therefore, the observed increase in propane ODH rates with Mo surface density is likely to reflect also the higher reducibility of larger MoO_x domains. The rate of reduction of MoO_x using H_2 can be probed using temperature-programmed reduction methods. Figure 9a shows reduction profiles for MoO_x/Al_2O_3 catalysts with Mo surface densities below 5 Mo/nm^2. The general features in these reduction profiles do not depend on the Mo surface density. Two broad peaks are detected below 1200 K. The low-temperature peak corresponds to the reduction of Mo^{6+} to Mo^{4+} and the high-temperature peak to the reduction of Mo^{4+} to Mo^0 (48, 49). The peak temperature for the first reduction decreased with increasing Mo surface density, suggesting that the reduction of Mo^{6+} to Mo^{4+} is faster on larger MoO_x domains.

The effects of O_2, C_3H_8, and H_2O concentrations on ODH rates on MoO_x-based catalysts, as well as *in situ* X-ray absorption measurements during reaction, have shown that oxygen anions and OH groups are the most abundant surface species and that oxygen vacancies are minority surface species (12). Therefore, it appears that the initial stages of the first reduction peak correspond to the reduction processes most relevant to ODH reactions. Figure 9b shows the reduction rate of Mo^{6+} to Mo^{4+} using H_2 as a function of temperature during the early stages of the Mo^{6+} reduction to Mo^{4+}. At a given temperature, the reduction rate increases with increasing Mo surface density. Figure 10 shows initial propane ODH rate constants at 703 K on MoO_x/Al_2O_3 catalysts with different Mo surface density plotted against the rate constant for MoO_x reduction in

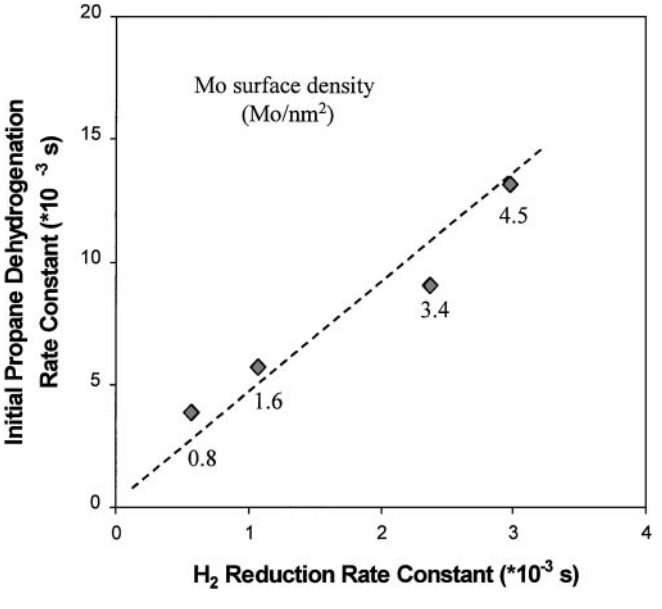

FIG. 10. Dependence of initial propene formation rate constant at 703 K on H_2 reduction rate constant at 673 K for MoO_x/Al_2O_3 catalysts.

H_2 at 673 K (H_2 reduction rate constants at 673 K from the data in Fig. 9b). The excellent correlation between these two properties is apparent from these data. Clearly, larger domains show weaker interactions between MoO_x and Al_2O_3 and they delocalize electrons more effectively; both effects lead to the more facile reduction of Mo centers and to a higher rate of C–H bond activation as the size of MoO_x domains increases.

The reducibility of MoO_x species with different domain size during treatment in H_2 and C_3H_8 was also examined by *in situ* X-ray absorption measurements. The reactant stream (20% H_2/Ar or 20% C_3H_8/He) was introduced at ambient temperature and the temperature was increased at 0.333 K s^{-1} to a specific temperature and then rapidly decreased to room temperature before the spectra were measured. Figures 11a and 11b show the spectra for MoO_x/Al_2O_3 catalysts after exposure to 20% H_2/Ar at RT, 723 K, and 823 K. Figures 12a and 12b show the corresponding spectra after exposure to 20% C_3H_8/He at RT, 723 K, and 823 K. A reference spectrum for MoO_2 is also included in Figs. 11 and 12. The spectrum for all samples approached that of MoO_2 as the temperature of exposure to H_2 or C_3H_8 reductants increases; the extent of reduction, however, differs among MoO_x/Al_2O_3 samples with surface densities between 0.4 and 4.5 Mo/nm^2. Below 823 K, Mo^{6+} and Mo^{4+} ions coexist in the MoO_x/Al_2O_3 sample and the near-edge spectrum can be described as a linear combination of the spectra for the starting material and for MoO_2. The relative concentrations of the two species, calculated from this linear combination approach (29, 50, 51), are shown in Figs. 13a and 13b, and a representative fit of a spectrum at intermediate extents of reduction is included in Fig. 11a for a sample

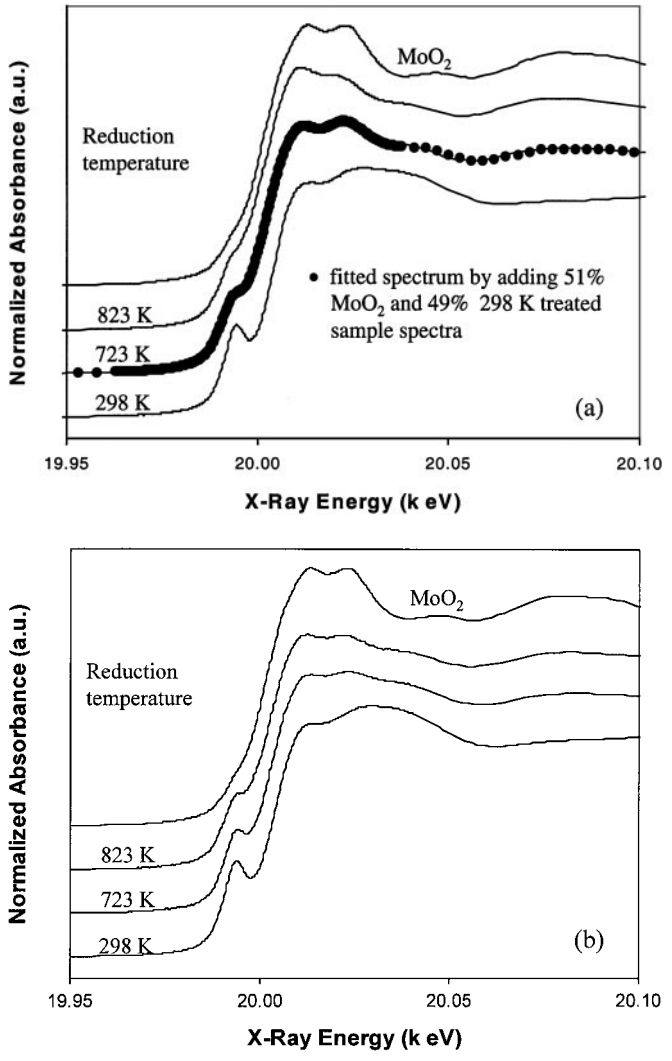

FIG. 11. Near-edge X-ray absorption spectra of reference compound MoO_2 and MoO_x/Al_2O_3 catalysts after treatment in 20% H_2/Ar at different temperatures: (a) 10% wt MoO_x/Al_2O_3 and (b) 6% wt MoO_x/Al_2O_3.

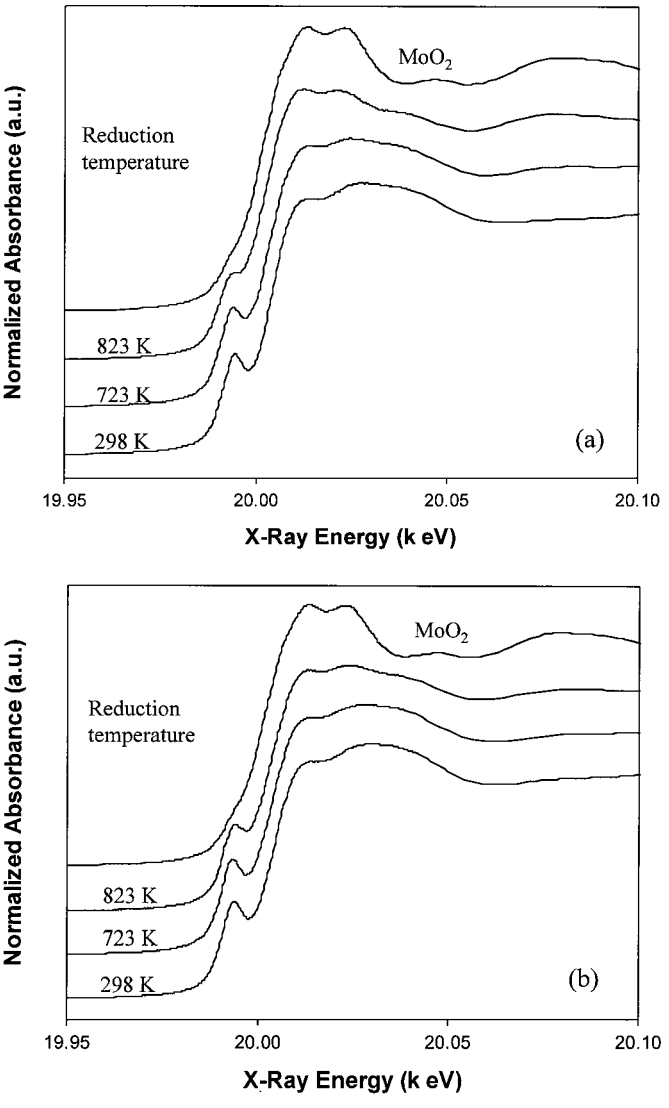

FIG. 12. Near-edge X-ray absorption spectra of reference compound MoO_2 and MoO_x/Al_2O_3 catalysts after treatment in 20% C_3H_8/He at different temperatures: (a) 10% wt MoO_x/Al_2O_3, and (b) 6% wt MoO_x/Al_2O_3.

containing nearly equimolar amounts of MoO_2 and of the initial structure. The excellent fit obtained confirms the appropriateness of this linear combination approach.

Figures 13a and 13b show the fraction of MoO_2 in MoO_3/Al_2O_3 catalysts with different Mo surface density after reduction at 723 or 823 K using 20% H_2/Ar and 20% C_3H_8/He, respectively. Clearly, a higher reduction temperature leads to more extensive reduction. At a given reduction temperature, the extent of reduction by H_2 or C_3H_8 increases with increasing Mo surface density, confirming that the reducibility of MoO_x species increases with increasing MoO_x surface density and domain size. Figure 14 shows the MoO_2 fraction in MoO_x/Al_2O_3 after reduction in 20% C_3H_8/He at 823 K and the initial propane ODH turnover rates at 703 K, both as a function of Mo surface density. The MoO_2 fraction increases in parallel with the observed increase in propane

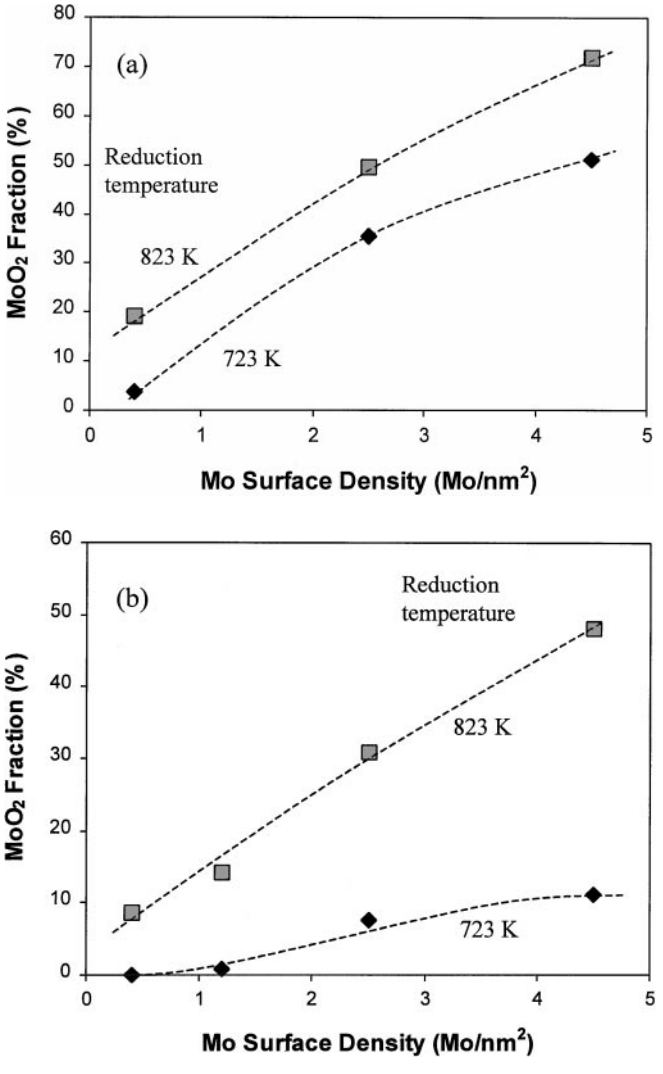

FIG. 13. Fraction of MoO_2 calculated from XANES fit in MoO_x/Al_2O_3 samples after reduction in (a) 20% H_2/Ar and (b) 20% C_3H_8/He at different temperatures.

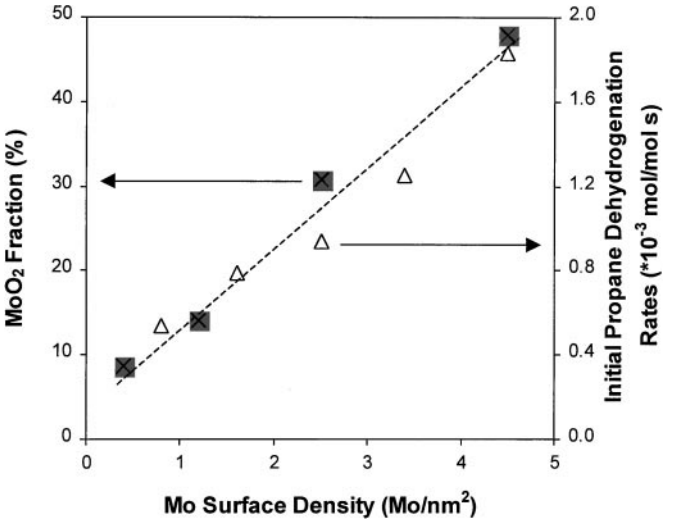

FIG. 14. Fraction of MoO_2 in MoO_x/Al_2O_3 catalysts after reduction in 20% C_3H_8/He at 823 K and the initial propane ODH rates (703 K, 14 kPa C_3H_8, 1.7 kPa O_2, balance He) as a function of Mo surface density.

ODH rates. The involvement of lattice oxygen in the rate-determining C–H bond activation steps for propane ODH reactions (11, 12) suggests that this transient measurement of the initial reduction process is relevant to the ability of these materials to be reduced during ODH reactions. These results also confirm that the increase of propane ODH reaction rates with increasing Mo surface density is caused by the easier reduction of larger MoO_x domains compared with smaller ones.

CONCLUSIONS

The structure of MoO_x species dispersed on Al_2O_3 depends strongly on the Mo surface density. Two-dimensional MoO_x oligomers are favored at Mo surface densities lower than those required for a polymolybdate monolayer (4.8 Mo/nm^2). At surface densities above 4.5 Mo/nm^2, polymolybdates and bulk phase MoO_3 coexist. For Mo surface densities between 0.4 and 12 Mo/nm^2, the size of two-dimensional and three-dimensional domains increased with increasing Mo surface density. At surface densities leading to the predominant presence of two-dimensional oligomers (<4.5 Mo/nm^2), propane ODH rates (per Mo atom) increased with increasing Mo surface density as a result of the higher reducibility of larger MoO_x domains. The reduction of Mo^{+6} centers and the generation of oxygen vacancies are involved in kinetically relevant elementary steps for propane ODH reactions on MoO_x-based catalysts. Higher surface densities ultimately lead to a decrease in propane ODH rates (per Mo atom), because the formation of three-dimensional MoO_3 structures leads to inaccessible Mo species. ODH areal rates (per BET surface area), however, approach a constant value with increasing surface density. This reflects the complete

coverage of Al_2O_3 with two- and three-dimensional MoO_x oligomers with similar surface reactivity in ODH reactions. Further increases in Mo surface density above 4.5 Mo/nm^2 lead to a lower propane ODH turnover rate because of the lower accessibility of Mo species caused by the formation of three-dimensional MoO_3 particles. Propene selectivities at zero reactant conversion increased with increasing Mo surface density up to ~5 Mo/nm^2 and then remained constant at higher surface densities. Similarly, propene combustion rates decreased relative to propane ODH rates with increasing Mo surface density. These effects suggest that the presence of Mo–O–Al surface sites favors the adsorption of propene and the combustion of the resulting alkoxide intermediates to form undesired CO_x products.

ACKNOWLEDGMENTS

This work was supported by the Director, Office of Basic Energy Sciences, Chemical Sciences Division, of the U.S. Department of Energy under Contract DE-AC03-76SF00098. X-ray absorption data were collected at the Stanford Synchrotron Radiation Laboratory, which is operated by the Department of Energy, Office of Basic Energy Sciences, under Contract DE-ACO3-76SF00515. The authors acknowledge Dr. George D. Meitzner, Chief Scientist, Edge Analytical, Inc., for his expert assistance with the acquisition and analysis of the X-ray absorption data and Mr. Kenny Komala for the acquisition and analysis of the UV-visible spectra.

REFERENCES

1. Blasko, T., and López Nieto, J. M., *Appl. Catal. A* **157**, 117 (1997).
2. Kung, H. H., *Adv. Catal.* **40**, 1 (1994).
3. Albonetti, S., Cavani, F., and Trifiro, F., *Catal. Rev. Sci. Eng.* **38**, 413 (1996).
4. Centi, G., and Triffiro, F., *Appl. Catal. A* **143**, 3 (1996).
5. Mamedov, E. A., and Cortés-Corberan, V., *Appl. Catal. A* **127**, 1 (1995).
6. Meunier, F. C., Yasmeen, A., and Ross, J. R. H., *Catal. Today* **37**, 33 (1997).
7. Cadus, L. E., Gomez, M. F., and Abello, M. C., *Catal. Lett.* **43**, 229 (1997).
8. Jalowiecki-Duhamel, L., Ponchel, A., and Barbaux, Y., *J. Chim. Phys. PCB* **94**, 1975 (1997).
9. Yoon, Y. S., Ueda, W., and Moro-oka, Y., *Topics Catal.* **3**, 256 (1996).
10. Lee, K. H., Yoon, Y. S., Ueda, W., and Moro-oka, Y., *Catal. Lett.* **46**, 267 (1997).
11. Chen, K., Khodakov, A., Yang, J., Bell, A. T., and Iglesia, E., *J. Catal.* **186**, 325 (1999).
12. Chen, K., Bell, A. T., and Iglesia, E., *J. Phys. Chem. B* **104**, 1292 (2000).
13. Khodakov, A., Olthof, B., Bell, A. T., and Iglesia, E., *J. Catal.* **181**, 205 (1999).
14. Khodakov, A., Yang, J., Su, S., Iglesia, E., and Bell, A. T., *J. Catal.* **177**, 343 (1998).
15. Chen, K., Xie, S., Iglesia, E., and Bell, A. T., *J. Catal.* **189**, 421 (2000).
16. Mestl, G., and Srinivasan, T. K. K., *Catal. Rev. Sci. Eng.* **40**, 451 (1998).
17. Zingg, D. S., Makovsky, L. E., Tischer, R. E., Brown, F. R., and Hercules, D. M., *J. Phys. Chem.* **84**, 2898 (1980).
18. Vuurman, M. V., and Wachs, I. E., *J. Phys. Chem.* **96**, 5008 (1992).
19. Kisfaludi, G., Leyrer, J., Knozinger, H., and Prins, R., *J. Catal.* **130**, 192 (1991).
20. Chan, S. S., Wachs, I. E., and Murrell, L. L., *J. Phys. Chem.* **88**, 5831 (1984).
21. Hu, H., Wachs, I. E., and Bare, S. R., *J. Phys. Chem.* **99**, 10897 (1995).
22. Imamura, S., Sasaki, H., Shono, M., and Kanai, H., *J. Catal.* **177**, 72 (1998).
23. Knozinger, H., and Jeziorowski, H., *J. Phys. Chem.* **82**, 2002 (1978).
24. Knozinger, H., and Ratnasamy, P., *Catal. Rev. Sci. Eng.* **17**, 31 (1978).
25. Xie, Y. C., and Tang, Y. Q., *Adv. Catal.* **37**, 1 (1990).
26. Chen, Y., and Zheng, L. F., *Catal. Lett.* **12**, 51 (1992).
27. Delgass, W. N., "Spectroscopy in Heterogeneous Catalysis," Academic Press, New York, 1979.
28. Barton, D. G., Ph.D. dissertation, University of California at Berkeley, 1999.
29. Ressler, T., WinXAS97, Version 1.2 (1998).
30. Weber, R. S., *J. Catal.* **151**, 470 (1995).
31. Tauc, J., in "Amorphous and Liquid Semiconductors" (J. Tauc, Ed.), Plenum, London, 1974.
32. Barton, D. G., Shtein, M., Wilson, R. D., Soled, S. L., and Iglesia, E., *J. Phys. Chem. B* **103**, 630 (1999).
33. Cherstnoy, N., Hull, R., and Brus, L. E., *J. Chem. Phys.* **85**, 2237 (1986).
34. Alivisatos, A. P., *Science* **271**, 933 (1996).
35. Service, R. F., *Science* **271**, 920 (1996).
36. Hoener, C. F., Allan, K. A., Bard, A. J., Campion, A., Fox, M. A., Mallouk, T. E., Webber, S. E., and White, J. M., *J. Phys. Chem.* **96**, 3812 (1992).
37. Bendoraitis, J. G., and Salomon, R. E., *J. Phys. Chem.* **69**, 3666 (1965).
38. Wang, Y., Mahler, S. W., and Kasowski, R., *J. Chem. Phys.* **87**, 7315 (1987).
39. Fournier, M., Louis, C., Che, M., Chaquin, P., and Masure, P., *J. Catal.* **119**, 400 (1989).
40. Meitzner, G. D., *Catal. Today* **39**, 281 (1998).
41. Shadle, E., Hedman, B., Hodgson, K. O., and Solomon, E. I., *Inorg. Chem.* **33**, 4235 (1994).
42. Aritani, H., Tanaka, T., Funabiki, T., Yoshida, S., Kudo, M., and Hasegawa, S., *J. Phys. Chem.* **100**, 5440 (1996).
43. Verbruggen, N. F. D., Mestl, G., von Hippel, L. M. J., Lengeler, B., and Knözinger, H., *Langmuir* **10**, 3063 (1994).
44. Takenaka, S., Tanaka, T., Funabiki, T., and Yoshida, S., *J. Phys. Chem. B* **102**, 2960 (1998).
45. Abello, M. C., Gomez, M. F., and Cadus, L. E., *Catal. Lett.* **53**, 185 (1998).
46. Albrecht, S., Wendt, G., Lippold, G., Adamski, A., and Dyrek, K., *Solid State Ionics* **101**, 909 (1997).
47. Grabowski, R., Grzybowska, B., Samson, K., Sloczynski, J., Stoch, J., and Wcislo, K., *Appl. Catal. A* **125**, 129 (1995).
48. Regalbuto, J. R., and Ha, J. W., *Catal. Lett.* **29**, 189 (1994).
49. Arnoldy, P., de Jonge, J. C. M., and Moulijn, J. A., *J. Phys. Chem.* **89**, 451 (1985).
50. Li, W., Meitzner, G. D., Borry, R. W., and Iglesia, E., *J. Catal.* **191**, 373 (2000).
51. Chen, K., Xie, S., Bell, A. T., and Iglesia, E., *J. Catal.* **195**, 244 (2000).